Discrete Adjoint Optimization of a Hypersonic Inlet

Kyle A. Damm,* Rowan J. Gollan,† Peter A. Jacobs,‡ and Michael K. Smart§
University of Queensland, Brisbane, Queensland 4072, Australia
and
Seonguk Lee,¶ Eunsa Kim,** and Chongam Kim††
Seoul National University, Seoul 151-742, Republic of Korea

Shape optimization of modern three-dimensional hypersonic inlets requires many geometric design parameters. Because the flow physics is complex, a Reynolds-averaged Navier–Stokes (RANS) analysis is also desirable when performing optimization. A computationally efficient means of handling many-parameter optimization with expensive cost functions is to use gradient-based searches informed by an adjoint flow solution. In this work, a discrete adjoint method for high-speed flows is documented. It is implemented in the open-source compressible-flow solver **Eilmer**. One difficulty with extending a hypersonic flow solver to include an adjoint solver is the differentiation of complex, nonlinear (and sometimes nondifferentiable) algorithms. Here, it is shown that difficulty can be overcome using flow Jacobians constructed with finite differences based on complex variables. The coupled flow and adjoint solvers are packaged together with a gradient-based optimizer. The flow and adjoint solvers are verified and validated for high-speed RANS analysis. The discrete adjoint method for optimization is demonstrated using the NASA P2 hypersonic inlet as a test case. The results show that the optimization method can remove an undesirable shock present in the original geometry, while achieving the desired compression ratio and improving overall performance metrics.

Nomenclature

A	=	cell area
$\boldsymbol{D}$	=	vector of design variables
d	=	dimension
f	=	discretized solution
f_{ref}	=	analytical manufactured solution
h	=	step size; also enthalpy
I	=	turbulence intensity
i	=	$\sqrt{-1}$
J	=	objective function
k	=	turbulent kinetic energy; also mesh refinement level
L	=	reference length
p	=	pressure; also observed order of accuracy
p_p	=	Pitot pressure
$p_{t,\infty}$	=	freestream stagnation pressure
$\boldsymbol{Q}$	=	vector of primitive variables
$\boldsymbol{q}$	=	vector of ghost cell primitive variables
$\boldsymbol{R}$	=	residual for a control volume
r	=	refinement factor
u, v	=	Cartesian velocity components
x, y	=	Cartesian spatial coordinates
ϵ	=	L_2 error norm
η	=	efficiency
λ	=	vector of adjoint variables
μ	=	dynamic viscosity
ρ	=	density
ϕ	=	general solution variable; also parameter in limiter
ω	=	turbulent frequency

Subscripts

ad	=	adiabatic
KE	=	kinetic energy
k	=	verification mesh level (1, 2, 3, etc., fine to coarse)
lam	=	laminar
p	=	Pitot
turb	=	turbulent
0	=	total flow condition
∞	=	freestream flow condition

*Ph.D. Candidate, Centre for Hypersonics, School of Mechanical and Mining Engineering.

†Lecturer, Centre for Hypersonics, School of Mechanical and Mining Engineering.

‡Reader, Centre for Hypersonics, School of Mechanical and Mining Engineering.

§Professor, Centre for Hypersonics, School of Mechanical and Mining Engineering.

¶Ph.D. Candidate, Department of Mechanical and Aerospace Engineering.

**Ph.D. Candidate, Department of Mechanical and Aerospace Engineering. Student Member AIAA.

††Professor, Department of Mechanical and Aerospace Engineering. Associate Fellow AIAA.

I. Introduction

THE drive for improved flexibility and reusability in satellite launch systems has brought resurgence in the popularity of scramjet-assisted access-to-space launch vehicle concepts. In addition to the superior specific impulse of scramjets over rockets, scramjet-powered accelerators have the advantage of operating like traditional aircraft. For this reason, scramjet-powered vehicles will offer better maneuverability, reusability, and a faster turn-around between launches [1]. A key challenge to designing a hypersonic accelerating scramjet engine is achieving robust combustion of the fuel–air mixture over a wide range of Mach numbers [2]. The design of the hypersonic inlet, which is required to provide desired flow conditions to the combustor, is consequently of considerable importance to achieving realizable scramjet-powered accelerators.

Present hypersonic inlet design methodologies integrate an inviscid flow analysis with boundary-layer correction techniques to achieve the desired flowfield compression. The P2 and P8 hypersonic inlets [3], developed in the 1970s at NASA, are an example of this procedure. The rectangular-to-elliptical-shape-transition (REST) inlet [4] is another, more modern example. Both of these classes of inlet have been known to suffer from adverse turbulent boundary-layer interactions, which are not evident during the design process [3,5].

Since the mid-1990s, a number of researchers have studied integrating high-fidelity Reynolds-averaged Navier–Stokes (RANS) calculations into the hypersonic inlet design process. Gelsey et al. [6] and Shukla et al. [7,8] presented some of the first RANS-based design optimization results for hypersonic inlets: throughout a series of

papers, the authors presented redesigns of the P2 and P8 hypersonic inlets using NASA's NPARC and GASP codes coupled with the k–ϵ turbulence model. Hasegawa and Knight [9,10] also used the GASP code in an automated design optimization of generic two-dimensional (2D) inlets using the k–ω turbulence model. More recently, Drayna [11] developed a sensitivity analysis code within the US3D solver and applied it to the design optimization of three-dimensional (3D) hypersonic inward turning inlets using the Spalart–Allmaras turbulence model. These referenced works all suffered from poor scalability for a large number of design parameters, in that for each additional design variable, at least one additional objective function evaluation was required. This poor scaling of the design iteration is too restrictive for practical hypersonic inlet design, considering that a 3D hypersonic inlet requires 50+ design parameters to capture the geometric detail [12].

A modern approach to computational fluid dynamics (CFD)–based optimization is the adjoint method [13]. The adjoint method enables the computation of all shape sensitivities for a given problem at the cost of only one flow solution and one adjoint solution. This is in contrast to other competing methods such as a direct sensitivity analysis, finite differences, or a direct complex variable approach, where the number of required flow solutions per design iteration scales with the number of design variables [14]. As a result of its efficiency, the adjoint method has become widely used for subsonic aircraft design, evolving to the application of full wing–body configurations [15]. In spite of the adjoint method's wide application to subsonic aircraft optimization, only the work by Kline et al. [16–20] has extended the method to hypersonic inlet design. The approach by Kline et al. applied the continuous adjoint method to optimize both 2D and 3D inlets using the RANS equations with the one-equation Spalart–Allmaras turbulence model. The alternative, discrete adjoint method, has not yet been explored in hypersonic inlet design, and that is one of the goals of the present work.

There are several advantages of the discrete adjoint approach. Foremost, the discrete approach first discretizes the set of equations before the differentiation. Because there exist algorithmic methods to linearize discretized equations, this suggests that the adjoint system construction procedure may be automated. This is not true for the continuous approach, which requires rederivation of the adjoint system for every new modification to the underlying set of equations. The discrete adjoint method can also be easily verified against a direct differentiation of the flow code, because the differentiation is of the discretized system. The continuous method does not have any theoretical equivalent, making verification difficult. Finally, as a result of the differences in the discretization related to the grid sensitivities, the continuous formulation may produce inaccurate gradients [14,21,22]. However, these inaccuracies have been shown to vanish as the mesh width is reduced [21,23].

Nielsen and Kleb [24] have implemented and verified an automated discrete adjoint method for 2D hypersonic flows. In their work, a spatially first-order Navier–Stokes flow code was linearized using complex variables. Their work built on the efforts by Anderson et al. [25] and Burdyshaw and Anderson [26], who implemented and verified a complex variable discrete adjoint method for 2D low-speed turbulent flows using the Spalart–Allmaras turbulence model. The advantage of constructing the linearization in this manner is that modifications to the flow solver are automatically accounted for in the adjoint solver [27]. The application of complex variable differentiation is the equivalent of applying forward-mode automatic differentiation, but it is much simpler to implement and maintain [28,29]. The linearization of the flow solver routines may also be automated by reverse-mode automatic differentiation. In small applications, it is sometimes possible to use automatic differentiation directly by feeding in a nonlinear code and obtaining a corresponding adjoint code [30]. However, typically for large solvers, applying automatic differentiation in a targeted or selective manner is necessary to achieve a code that is both computationally efficient and memory efficient [31–34]. Additionally, the applicability of automatic differentiation depends on the availability of robust third-party automatic differentiation libraries that can parse the baseline flow solver programming language. For these reasons, in the current work,

a complex variable approach is used to linearize a spatially second-order RANS flow code with the k–ω turbulence model. The coupled flow and adjoint solvers are packaged together with a gradient-based optimizer to perform hypersonic inlet design optimization. The major contribution of this work is description and application of an adjoint solver in high-speed compressible flow optimization. Specifically, the work reported here shows how to use complex-step differentiation to linearize a second-order unstructured RANS solver. We believe that the complex-step approach is easy to implement, and competitive with other approaches on accuracy and efficiency.

The rest of the paper is as follows: Sec. II introduces the P2 hypersonic inlet, which will be the example problem for this work. Section III will introduce the flow solver used for this work, in addition to presenting a verification and validation for hypersonic inlet flows. Section IV will present the shape optimization methodology applied for this optimization work, including a detailed description of the adjoint solver implementation, shape parameterization, mesh movement strategy, and verification of the adjoint sensitivities. Section V will then present the design optimization results for the P2 hypersonic inlet. Conclusions and future research suggestions are presented in Sec. VI.

II. P2 Hypersonic Inlet

We have selected to redesign the P2 hypersonic inlet to demonstrate the applicability of the discrete adjoint method to hypersonic inlet design. This problem has been previously used to demonstrate the use of black-box finite-difference-style CFD optimization for hypersonic inlet design [6–8], and, consequently, the inlet design community has some familiarity with the geometry. The P2 inlet (illustrated in Fig. 1) was a 2D, planar, hypersonic inlet designed for a generic accelerating vehicle at NASA in the early 1970s [3]. The original design objective was to achieve a desired compression ratio of 2 across the cowl shock while providing an approximately uniform static pressure distribution at the throat. From the experimental campaign, it was observed that the inlet did not achieve a uniform static pressure distribution across the throat. Instead, the cowl shock reflected off the body side of the inlet rather than being canceled by an expansion. Gnos et al. [3] attributed the failure of the design approach to the analytical technique's poor capturing of the various interactions between the viscous and inviscid components of the flow and, in particular, the turbulent shock-wave–boundary-layer interaction. Our goal in this work is to show how discrete adjoint optimization can be used to develop a correction to the inlet shape that delivers on the original design intent.

III. Flow Solver

A. Description

The flow solver used in this work is the open-source compressible-flow CFD code `Eilmer` [35], developed at the University of Queensland's Centre for Hypersonics. `Eilmer`, written in the D programming language [36], uses a finite volume method to solve the Euler, Navier–Stokes, or RANS equations on either structured or unstructured, two- or three-dimensional body-fitted grids using explicit time integration or Newton–Krylov acceleration for steady-state problems. The flow solutions obtained in this current work
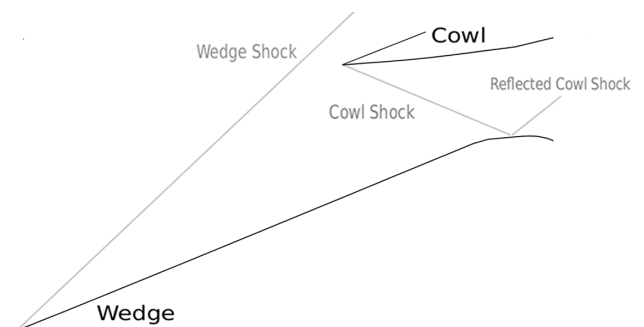

Fig. 1   Schematic of the P2 hypersonic inlet.

employ Eilmer's unstructured steady-state solver. The residual function for a cell in Eilmer, discretized by the finite volume method, is given by

$$R = -\frac{1}{V} \sum_{\text{faces}} (\overline{F_c} - \overline{F_v}) \cdot \hat{n} \, dA + S \qquad (1)$$

where V is the cell volume, S is the cell-averaged source terms, F_c are the convective fluxes, F_v are the viscous fluxes, and $\sum_{\text{faces}}$ denotes integration over the cell interfaces. The convective fluxes (F_c) are computed using the AUSMDV scheme by Wada and Liou [37]. Second-order spatial accuracy for convective fluxes is achieved by reconstructing the primitive flow state variables (u, v, ρ, p, k, ω) within the finite volumes using an unweighted least-squares method with a nearest-face-neighbor stencil [38]. To ensure stability when reconstructing the flow state in finite volumes near strong shocks, the limiter by Venkatakrishnan is employed [39]. The spatial gradients required at the cell interface midpoints for computing the viscous fluxes (F_v) are computed using a cell-centered weighted least-squares method and the face-tangent-augmented face-gradient method [40]. The Reynolds stresses in the RANS equations are modeled using Wilcox's 2006 $k–\omega$ turbulence model [41]. The use of AUSMDV in conjunction with the $k–\omega$ turbulence model has been shown to provide accurate results for hypersonic flows, representative of those experienced by hypersonic inlets [42,43]. For the calculations in this work, the system is closed using the ideal gas equation of state. A Jacobian-free Newton–Krylov method is used for acceleration to steady state [44]. A preconditioned, restarted GMRES method is used to solve the system of linear equations arising when solving for the Newton steps [45]. Robust preconditioning is achieved by an incomplete lower-upper (LU) factorization of an approximate flow Jacobian constructed by only considering a nearest-face-neighbor stencil, ILU[0]. The Jacobian is constructed numerically using the procedure outlined in Sec. IV. To reduce the computational cost of constructing the preconditioner matrix, the Jacobian is frozen for a user-selectable number of iterations. For this work, the Jacobian was frozen for 100 iterations. Convergence is further accelerated by applying grid sequencing, starting with a coarse grid and moving the solution to a finer grid once it has converged.

B. Verification

The flow solver has been verified using the Method of Manufactured Solutions (MMS) [46]. MMS is a code verification technique that can be used to assess the order of accuracy of a computational fluid dynamics code. An extensive description of the method can be found in the textbook by Oberkampf and Roy [47] and is not repeated here. The chosen analytical solution for this work was first presented by Roy et al. [48] and is shown in Eq. (2). The constants are given in Table 1. Because we are interested in RANS simulations of the hypersonic inlet, the RANS equation formulation in Eilmer is the subject of verification. The gas is modeled as a calorically perfect gas with $\gamma = 1.4$, $R = 287.0 \text{ J}/(\text{kg} \cdot \text{K})$, $\mu = 10.0 \text{ Pa} \cdot \text{s}$, $Pr = 1.0$, and $Pr_T = 0.89$.

$$\phi(x,y) = \phi_0 + \phi_x \sin\left(\frac{a_{\phi x} \pi x}{L}\right) + \phi_y \cos\left(\frac{a_{\phi y} \pi y}{L}\right) + \phi_{xy} \cos\left(\frac{a_{\phi xy} \pi x y}{L^2}\right) \qquad (2)$$

The L_2 norm was used to determine the order of accuracy, defined as

$$\epsilon = \|f - f_{\text{ref}}\|_2 = \left(\frac{1}{N} \sum_{n=1}^{N} |f_n - f_{\text{ref},n}|^2\right)^{1/2} \qquad (3)$$

where f is the discretized solution and f_{ref} is the analytical manufactured solution. The order of accuracy is estimated by the following equation:

$$p = \frac{\ell_n(\epsilon_{k+1}/\epsilon_k)}{\ell_n(r)} \qquad (4)$$

where ϵ_{k+1} is the error at the coarse level and ϵ_k is the error at the fine level, and

$$r = \left(\frac{N_k}{N_{k+1}}\right)^{1/d} \qquad (5)$$

Here the refinement factor r is defined as the ratio of the number of cells in a mesh at level k (N_k) and a coarse mesh at level $k + 1$ (N_{k+1}) raised to the power of $1/d$, where d is the dimension (i.e., 2 for two dimensions).

The levels of grid refinement used in this study are presented in Table 2. We have used 4×4 blocks across the square domain for the results presented in this paper.

The results from the MMS test are presented in Figs. 2a and 2b. The flow solver achieves the expected second order of spatial accuracy in all flowfield primitives. Here we show the results for turbulent kinetic energy (k) and turbulent frequency (ω). The manufactured solution used in the verification procedure above was smoothly varying. To assess the spatial order of accuracy in the presence of discontinuities, the Method of Exact Solutions [47] was employed. The chosen flowfield was that of an oblique shock resulting from a Mach 3, inviscid gas ($\gamma = 1.4$) impinging on a 15 deg wedge. This particular flow configuration was chosen because an analytical solution exists [49]. For this verification case, the flow solver spatial accuracy is reduced to approximately first order ($p \approx 0.95$) as a result of the gradient limiting near the shock, as measured by the L_1 norm in all flowfield primitives.

C. Validation

The flow solver has been validated for use in this inlet design context by comparison to the original experimental results of the P2 inlet presented by Gnos et al. [3]. The sharp cowl approximation presented by Knight [50] is applied in this work to reduce the computational complexity of resolving the blunt leading edge. The P2 inlet walls were modeled as no slip boundaries with a fixed temperature of 304 K, consistent with what was reported by the experimenters [3]. The inflow conditions were computed from the reported stagnation conditions, assuming $\gamma = 1.4$ for ideal air, and are presented in Table 3. No experimental data quantifying the turbulence intensity of the freestream are available for this inlet. Consequently, several combinations of freestream turbulence intensity and eddy viscosity ratio were applied, and are presented in Table 4. Transition was modeled by separating the domain into a laminar region and a turbulent region. The turbulent region was set at

Table 1 Constants for $k–\omega$ Reynolds-averaged Navier–Stokes manufactured solution

Flow variable, ϕ	ϕ_0	ϕ_x	ϕ_y	ϕ_{xy}	$a_{\phi x}$	$a_{\phi y}$	$a_{\phi xy}$
ρ, kg/m³	1	0.15	−0.1	0.08	0.75	1	1.25
u, m/s	70	7	−8	5.5	1.5	1.5	0.6
v, m/s	90	−5	10	−11	1.5	1	0.9
p, N/m²	1×10^5	0.2×10^5	0.175×10^5	-0.25×10^5	1	1.25	0.75
k, m²/s²	780	160	−120	80	0.65	0.7	0.8
ω, 1/s	150	−30	22.5	40	0.75	0.875	0.6

Table 2 Levels of grid refinement used for verification

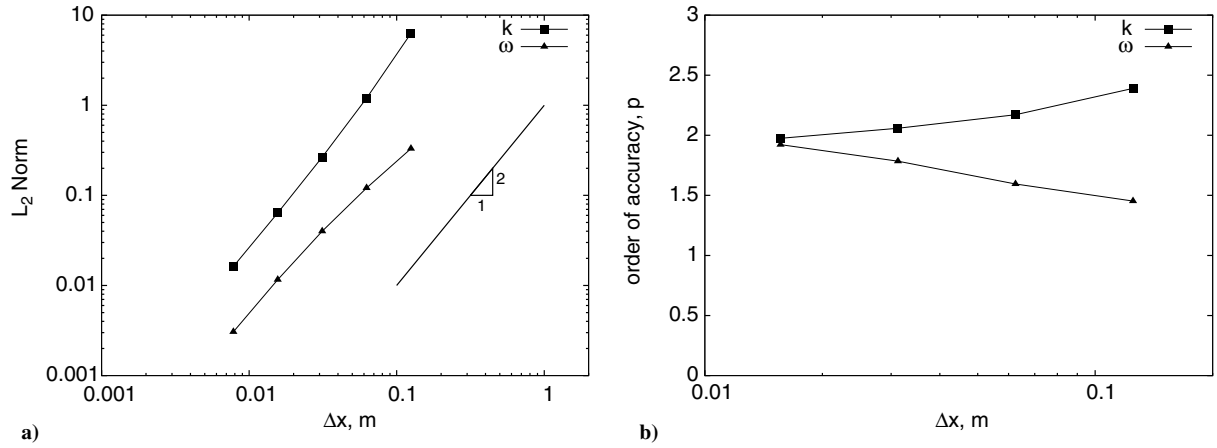| Grid	Dimensions	Cell width, Δx, m
1	8×8	0.125
2	16×16	0.0625
3	32×32	0.03125
4	64×64	0.015625
5	128×128	7.8125×10^{-3}

Fig. 2   a) L_2 error norm for turbulent kinetic energy (k) and turbulent frequency (ω). b) Order of accuracy based on L_2 error norm.

a distance of 40% of the fore-body wedge length. This distance matched that observed in experiment. First-order extrapolation of the flow state is applied at outflow boundaries. A grid independence study was undertaken, consisting of three levels of refinement, tabulated in Table 5. The G2 grid is presented in Fig. 3. Each mesh achieves a $y+$ of less than 1 along the inlet body-side wall, except G1, which has a maximum $y+$ of 1.2 near the reflected shock region. The simulations were considered converged once the global residual was reduced by at least eight orders of magnitude. Mesh sequencing was used to accelerate convergence, with the current grid level being initialized with the previous grid level's converged solution. The G1 grid was initialized with the freestream condition and a fake boundary layer, generated by a blending of the wall properties and freestream conditions over 25 cells normal to the wall.

Figure 4 presents pressure contours for the converged solution on grid G3 for simulation S3. The strong reflected cowl shock observed in the experimental campaign is also present in the RANS calculation. Annotated on Fig. 4 are three stations at which pressure probes were placed during the experiment. The Pitot pressure at each station for simulation S3 is compared with the experimental data from Gnos et al. [3] in Figs. 5a–5c. Similar grid convergence trends were observed for simulations S1, S2, and S4; however, for brevity, the results are omitted. The results for simulations S1–S4, on grid G3, are presented in Figs. 6a–6c. For all simulations, the largest discrepancy is noticeable near the cowl surface, where the sharp cowl approximation has not captured the entropy layer generated by the blunt leading edge. It is evident that the core flow of the inlet is sensitive to the inflow freestream turbulence properties. Along the body side of the inlet, our simulations are in good agreement with the experimental data in the boundary-layer region; however, an overprediction in the core-flow region is observed. The numerical results compare well with others who have applied the sharp cowl approximation; however, prior works did not notice an overprediction of the normalized Pitot pressures in the core flow [6–8,50]. These authors used a patched-grid approach by dividing the inlet into self-contained regions, in comparison to simulating the inlet in a tip-to-tail fashion, as done in this current work. An overprediction of core-flow Pitot pressure has been reported for tip-to-tail simulations of the P8 hypersonic inlet by several authors [51], tested during the same experimental study [3]. Despite this sensitivity, the major flow features are captured by the flow solver, and hence the simulations will serve their purpose of demonstrating adjoint-based inlet design in the present work.

IV.   Optimization Methodology

The gradient-based optimization methodology applied in this work is separated into five distinct steps: 1) geometry parameterization; 2) mesh generation and deformation; 3) gradient evaluation; 4) objective function evaluation, or in the context of CFD-based optimization, flow solution evaluation; and 5) numerical optimization. Step 4 was covered in Sec. III. The remaining steps are the topic of this section. We begin the section with a detailed description of our implementation of the discrete adjoint method for evaluating the shape sensitivities used in the gradient-based optimization. A brief presentation of the geometry parameterization, mesh movement, and numerical optimizer used in this work is then presented. The section concludes with a verification of the adjoint sensitivities by comparison to a direct complex variable method.

A.   Gradient Evaluation

1.   Discrete Adjoint Sensitivity

We consider here an adjoint system in the context of an optimization problem that seeks to minimize objective function J. There are several approaches to deriving the discrete adjoint system. Here we present an approach using Lagrange multipliers. First, the objective function, $J(Q(D), X(D))$, is reformulated as a Lagrangian function:

$$L(Q(D), X(D), \lambda) = J(Q(D), X(D)) + \lambda^T R(Q(D), X(D)) \quad (6)$$

where Q is the vector of flow state variables, D is the vector of design variables, X are the grid points, R is the residual vector [defined in Eq. (1)], under the assumption that the flow is at steady state, i.e.,

Table 3   Freestream inflow conditions for P2 inlet

Mach	7.4
Velocity, m/s	1221.8
Pressure, Pa	701.4
Temperature, K	67.85

Table 4   Freestream turbulence properties for P2 inlet

Simulation	I	$\mu_{\mathrm{lam}}/\mu_{\mathrm{turb}}$
S1	0.03	10
S2	0.03	100
S3	0.04	10
S4	0.05	10

Table 5   Levels of grid refinement used for validation

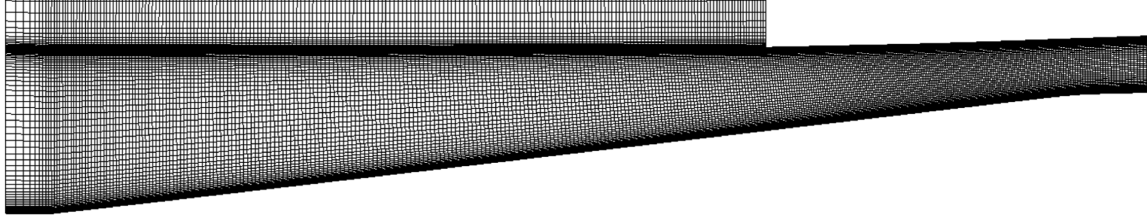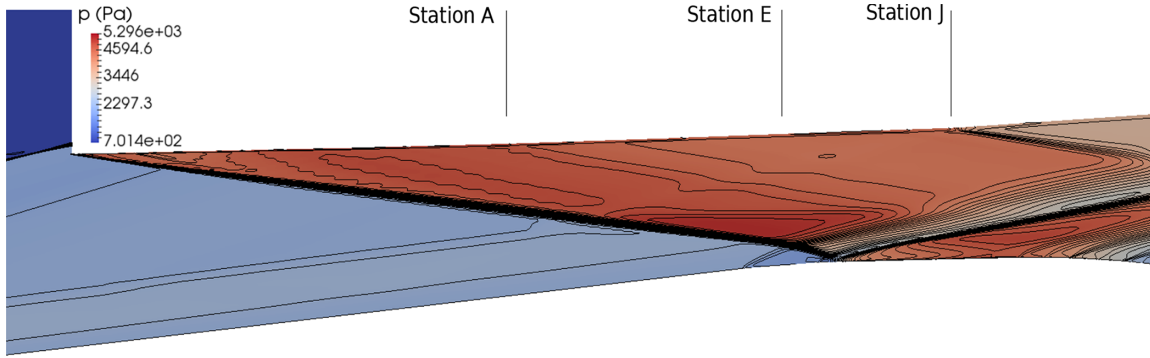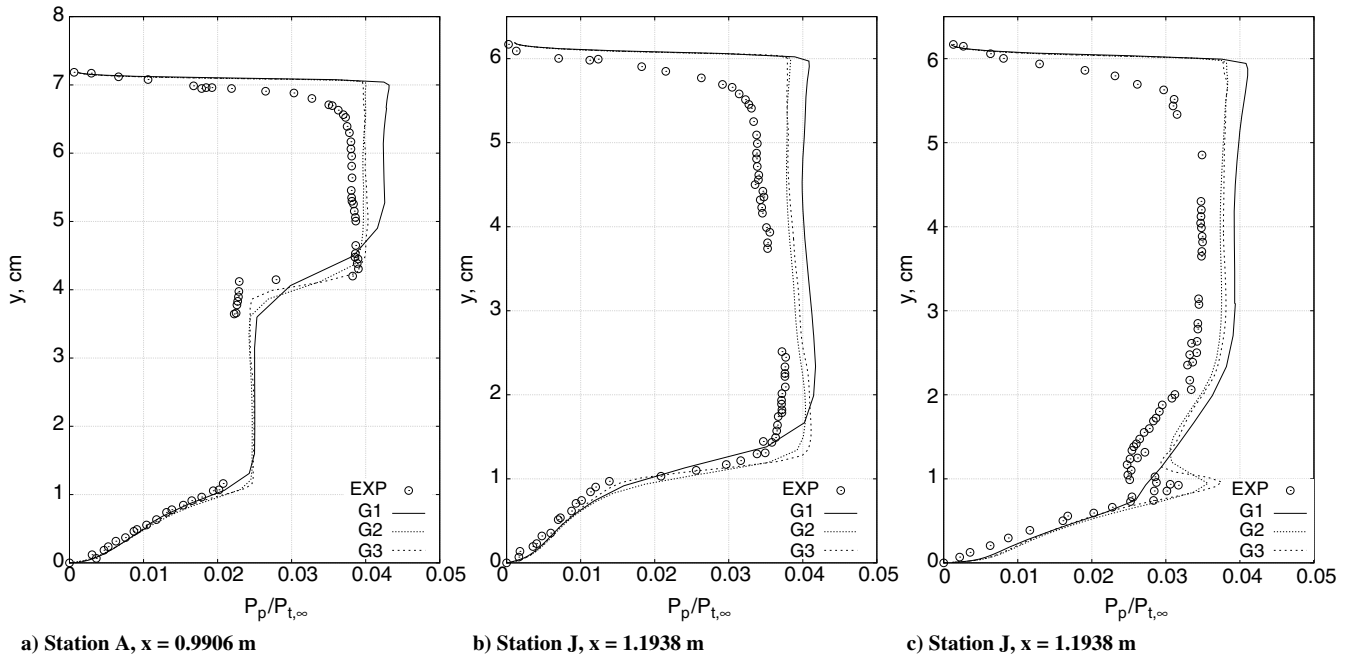| Grid	No. of cells
G1	16,240
G2	66,125
G3	266,845

Fig. 3   P2 inlet grid level G2.

Fig. 4   Baseline P2 inlet pressure color map and contour lines for simulation S3 on grid level G3, with annotated experimental measurement locations.

a) Station A, x = 0.9906 m   b) Station J, x = 1.1938 m   c) Station J, x = 1.1938 m

Fig. 5   Simulation S3 Pitot pressure (P_P), normalized by $P_{t,\infty} = 4.14$ MPa. Experimental data from [3].

$$R(Q(D), X(D)) = 0 \qquad (7)$$

and λ are the adjoint variables. By applying the chain rule, the sensitivity of this Lagrangian function with respect to the design variables is given as follows:

$$\frac{dL}{dD} = \frac{\partial J}{\partial X}\frac{dX}{dD} + \left(\frac{\partial J}{\partial Q} + \lambda^T \frac{\partial R}{\partial Q}\right)\frac{dQ}{dD} + \lambda^T \frac{\partial R}{\partial X}\frac{dX}{dD} \qquad (8)$$

The sensitivity of the flow state variables with respect to the design variables, dQ/dD, is computationally expensive to compute, and the goal of the adjoint method is to remove it from the sensitivity calculation. Given that the residual of the Navier–Stokes equations at steady state is zero (because they are a set of conservation

equations), the adjoint variables may take any arbitrary value. The adjoint variables are chosen to eliminate the dQ/dD term in Eq. (8) by setting

$$\left(\frac{\partial J}{\partial Q} + \lambda^T \frac{\partial R}{\partial Q}\right) = 0 \qquad (9)$$

this is more commonly written as the adjoint equation

$$\left(\frac{\partial R}{\partial Q}\right)^T \lambda = -\left(\frac{\partial J}{\partial Q}\right)^T \qquad (10)$$

The objective function sensitivity is then given by

a) Station A, x = 0.9906 m   **b) Station J, x = 1.1938 m**   **c) Station J, x = 1.1938 m**
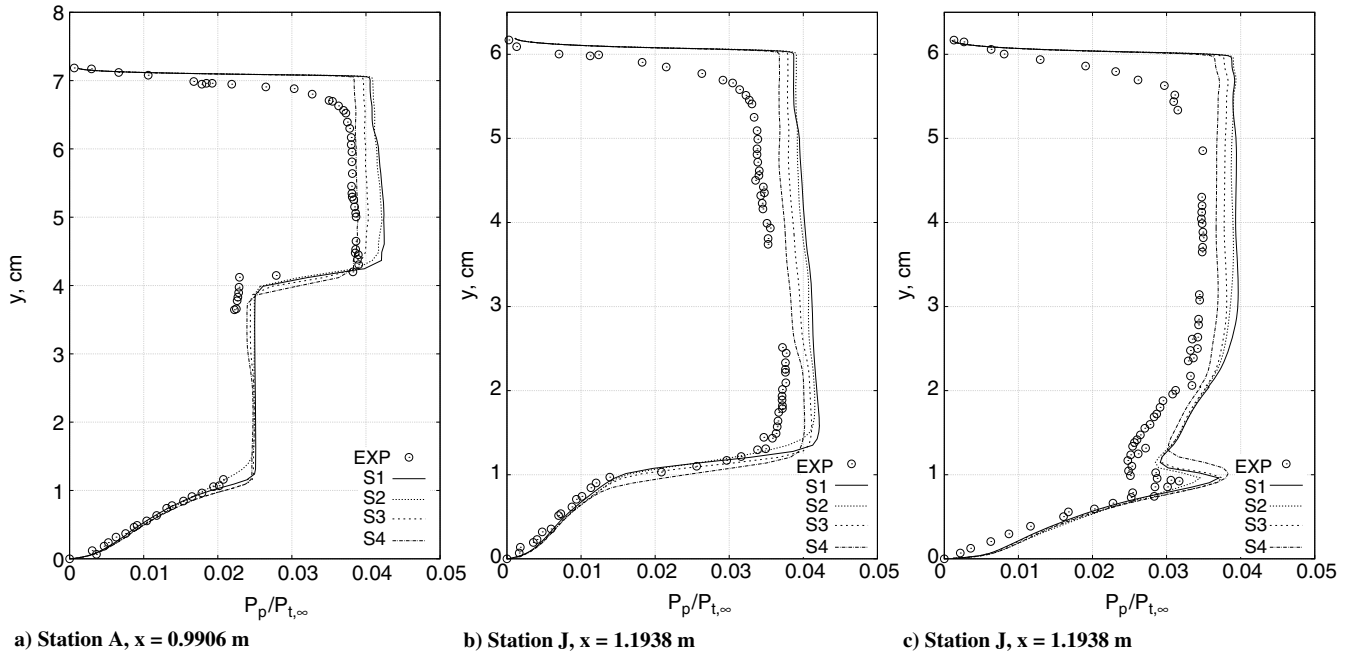
Fig. 6 Simulation S3 on level G3 Pitot pressure (P_P), normalized by $P_{t,\infty} = 4.14$ MPa. Experimental data from [3].

$$\frac{dL}{dD} = \frac{\partial J}{\partial D} + \lambda^T \frac{\partial R}{\partial D} \qquad (11)$$

where

$$\frac{\partial R}{\partial D} = \frac{\partial R}{\partial X} \frac{dX}{dD} \qquad (12)$$

and

$$\frac{\partial J}{\partial D} = \frac{\partial J}{\partial X} \frac{dX}{dD} \qquad (13)$$

Equation (11) is independent of dQ/dD. As a consequence, it is significantly less computationally expensive to evaluate than Eq. (8). The computation of the objective function gradient thus requires the exact linearization of the residual vector ($[\partial R/\partial Q]^T$), the evaluation of the remaining partial derivatives ($\partial J/\partial D$, $\partial R/\partial D$, $\partial J/\partial Q$), and the solution of the adjoint system of equations for the adjoint variables (λ).

2. Implementation

a. Residual Vector Linearization. In `Eilmer`, we use complex variables [52] to construct the exact linearization of the residual vector. The approach is similar to applying real-valued finite differences [53]; however, as no subtraction operator is required, this eliminates the subtractive cancellation error that severely limits the accuracy of

the real-valued approach [52]. Consequently, the perturbation size can be selected appropriately small enough based solely on truncation error considerations.

When applying the complex variable approach to linearize the residual vector, a primitive flow variable is perturbed along the imaginary axis in the complex plane by some perturbation size h, the flow solver residual routine is then executed, and the imaginary part is mined to evaluate one entry of the matrix, as shown in Eq. (14) for the kth residual vector entry and jth primitive flow variable. In this approach, by looping through all primitive variables (u, v, ρ, p, k, ω), over all cells, the transposed Jacobian matrix $[\partial R/\partial Q]^T$ is constructed row by row and stored in compressed row storage (CRS) format as outlined by Saad [45].

$$\frac{\partial R_k}{\partial Q_j} = \frac{Im[R_k(Q_j + ih)]}{h} \qquad (14)$$

To improve efficiency, the residual is only evaluated on a subset of cells that are contained in what we refer to as the residual stencil. The residual stencil is composed of all cells that will have an imaginary contribution from a perturbation of a particular cell. The residual stencil for the Euler equations in two dimensions is illustrated in Fig. 7. Although this example uses a structured arrangement of elements, the solver works on unstructured grids and is not limited to quadrilateral or hexahedral cells.
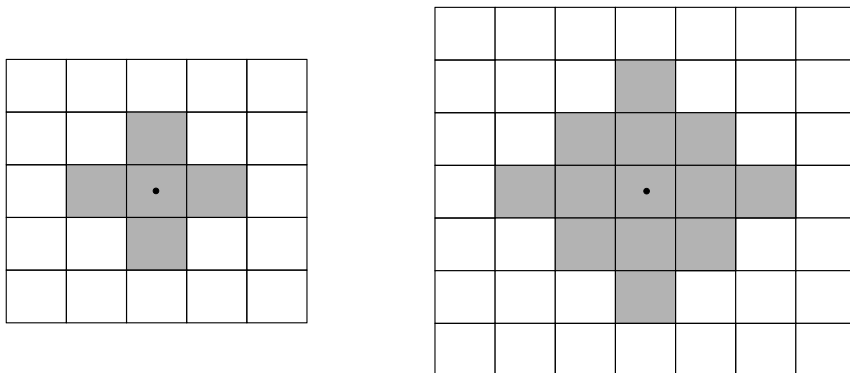

Fig. 7 Residual stencil: first order (left) and second order (right). (·) denotes perturbed cell.

b. Parallelization. The construction of the Jacobian is parallelized using the same domain decomposition as the flow solver. Following the approach by Saad [54] for solving linear systems on decomposed domains on distributed systems, each block in the decomposition stores a local Jacobian matrix (A_{loc}) and an external Jacobian matrix (A_{ext}), illustrated in the schematic presented as Fig. 8. The local Jacobian matrix is a square matrix that stores the sensitivities of local cell residuals from perturbations of local cell primitive variables. The external Jacobian matrix is a nonsquare matrix that stores all the entries for perturbations of local cells that effect the residual calculation of cells in neighboring blocks. To achieve an exact linearization for second-order spatially accurate simulations using a nearest-neighbor least-squares approach, the Jacobian routine requires one extra layer of ghost cells at block connections than the flow solver, as shown in Fig. 8.

c. Boundary Conditions. Boundary conditions in the adjoint solver must be handled explicitly [55]. The explicit boundary conditions for the Jacobian can be written as Eq. (15), where $\boldsymbol{R}$ and $\boldsymbol{Q}$ are as defined above, and $\boldsymbol{q}$ represents the ghost cell flow state variables.

$$\frac{\partial \boldsymbol{R}}{\partial \boldsymbol{Q}} = \left.\frac{\partial \boldsymbol{R}}{\partial \boldsymbol{Q}}\right|_{\mathrm{int}} + \frac{\partial \boldsymbol{R}}{\partial \boldsymbol{q}}\frac{\partial \boldsymbol{q}}{\partial \boldsymbol{Q}} \qquad (15)$$

The second term in Eq. (15) represents the application of the physical boundary conditions. The sensitivity $[\partial \boldsymbol{R}/\partial \boldsymbol{q}]$ is simply the resultant perturbation of the residual vector entry from a perturbation of a ghost cell flow state variable. It may be formed using a similar approach as the internal cells. The second sensitivity, $[\partial \boldsymbol{q}/\partial \boldsymbol{Q}]$, can be thought of as a transform from the internal flow state to the ghost cell flow state. This transform can be evaluated using the complex variable method, by perturbing an internal cell's flow state, applying the physical boundary condition, and mining the complex part of the ghost cell flow state. To improve efficiency for applying adjoint boundary conditions in `Eilmer`, our physical boundary conditions may be applied on a per-interface basis. To provide an exact linearization of the flow solver, the physical interfacial boundary condition information should be communicated to neighboring blocks during the construction of the external Jacobian matrix (A_{ext}). To simplify the implementation, the communication of this information is omitted in `Eilmer`. Although this omission results in some small error in several entries of the Jacobian, the effect is limited to only those entries where a physical boundary condition is intersected by a block-to-block boun-

dary condition, i.e. in the corners of the decomposed domains. In Sec. IV.C, it is shown that this simplification does not substantially reduce the accuracy of the adjoint sensitivities.

d. Frozen Limiter. A known problem for supersonic and hypersonic flow codes is that the limiters, necessary to ensure stability, can oscillate, causing a stalling of the convergence. This is sometimes referred to as limiter ringing [56,57]. The level of convergence achieved before stalling is problem dependent. Because the adjoint method is predicated on the assumption that the residual vector has been reduced to machine precision [see Eq. (7)], performing an adjoint solve on a stalled flowfield residual can cause the adjoint solver to either diverge, or converge on an inaccurate solution. Furthermore, the routines in the flow code that evaluate the limiter values have been observed to be sensitive to complex variable perturbations [56]. This has also been observed in this current work. One approach to overcome this limitation is to freeze the limiter after stalled convergence [58]. In this approach, once convergence has stalled, the limiter value for each cell is frozen; i.e., the limiter value is no longer re-evaluated, but is still applied. When applying the Venkatakrishnan limiter [39], a scalar value (ϕ) for each primitive flow state variable is calculated and stored at the cell centers. The flowstate reconstruction with gradient limiting is then evaluated as

$$Q_{j+1/2} = Q_j + \phi \cdot \nabla Q_j \cdot \frac{1}{2}\Delta \boldsymbol{x}_{jk} \qquad (16)$$

where $j+1/2$ denotes a cell interface, and $\boldsymbol{x}_{jk}$ is the cell-center position vector that points from cell j to cell k. When the limiter is frozen, ϕ is no longer re-evaluated; however, Eq. (16) is still employed during the reconstruction procedure using the frozen values. Thompson [56] applied this approach for the Van Albada [59] and Van Leer [60] limiters, in the context of high-speed adjoint optimization. In this context, the adjoint solver does not recompute the limiter values when constructing the Jacobian, but, instead, uses the frozen limiter values from the flow solver.

e. Numerical Solution of the Adjoint Equations. In addition to the adjoint operator detailed in the previous section, the right-hand side of the adjoint system of equations requires the formation of the partial derivative of the objective function with respect to the flow state variables, $\partial J/\partial \boldsymbol{Q}$. Entries from this partial derivative are evaluated by perturbing each flow state variable sequentially in the complex
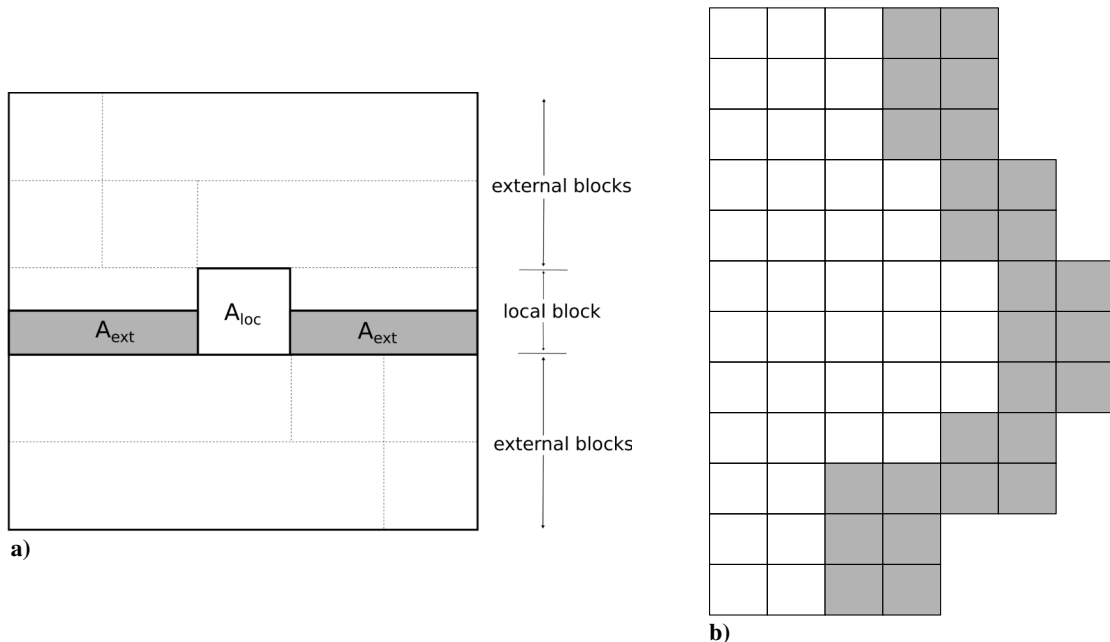

Fig. 8 a) Domain-decomposed Jacobian. b) Domain-decomposed block–block boundary. Shaded cells are cells from the neighboring block required in the external Jacobian construction.

domain, and executing the objective function routine. The imaginary part of the objective function is then mined to construct the sensitivity vector. Because this vector is typically filled with mostly zeros, to improve efficiency, it is possible to perform targeted differentiation. In this approach, only flow states in cells that will affect the objective function are perturbed, and the remaining entries are automatically filled with zero entries. For example, if the objective function is drag along a boundary, then only cells near the boundary need explicit evaluations of the perturbed objective function routine. The resulting linear system is solved using a preconditioned, restarted GMRES method, as per the flow solver outlined in Sec. III. Preconditioning of the system is accomplished by an incomplete LU factorization of a first-order Jacobian matrix using zero fill-in, ILU[0]. Details are found in the book on iterative methods by Saad [45].

f. Remaining Partial Derivatives. To perform the total derivative calculation [Eq. (11)] requires forming additional partial derivatives: $\partial \boldsymbol{R}/\partial \boldsymbol{D}$ and $\partial J/\partial \boldsymbol{D}$. The residual vector partial derivative, $\partial \boldsymbol{R}/\partial \boldsymbol{D}$, is evaluated by perturbing each design variable sequentially in the complex plane, executing the mesh deformation routine (outlined in Sec. IV.B), and then evaluating a flow solver residual routine over the entire flow domain. The imaginary part of the residual vector entries is then mined to construct the sensitivity matrix. So for n design variables, n residual evaluations are required. This is still typically a small cost compared with the number of residual evaluations required to converge a flowfield calculation. The remaining partial derivative with respect to the design variables, $\partial J/\partial \boldsymbol{D}$, is evaluated similarly, by perturbing each design variable sequentially in the complex plane, executing the mesh deformation routine and then evaluating the objective function routine. In practice, the code performs the following steps for each of the n design variables:

1) Perturb design variable D_j in the complex plane.
2) Execute surface parameterization routine:
    ⇒ Sensitivities are propagated to the mesh nodes along the parameterized surface.
3) Execute mesh deformation routine:
    ⇒ Sensitivities are propagated to all mesh points.
4) Execute flow solver residual routine:
    ⇒ Sensitivities are propagated to conserved residual quantities.
5) Evaluate $\partial \boldsymbol{R}/\partial D_j$.
6) Execute objective function routine:
    ⇒ Sensitivities are propagated to the objective function scalar quantity.
7) Evaluate $\partial J/\partial D_j$.

In this way only n calls to the mesh deformation routine are required.

B. Shape Parameterization, Mesh Movement, and Numerical Optimizer

All design surfaces in this work are parameterized with n-order Bézier curves. Each Bézier control point has a fixed x coordinate and a variable y coordinate. Perturbations of the Bézier control points

require consistent perturbations of the internal mesh points. The mesh movement is evaluated using inverse distance weighting. This approach has been shown to produce mesh qualities comparable to alternate methods at a fraction of the computational cost [61]. The initial meshes have been generated using the Pointwise software and domain decomposition of the mesh is achieved via METIS [62]. The gradient evaluation routines in `Eilmer` are coupled to the open-source optimization software DAKOTA [63]. The Fletcher–Reeves Conjugate Gradient (FRCG) method [64] has been used in the optimization study presented in Sec. V. FRCG is a method for solving unconstrained, nonlinear optimization problems. Constraints may be handled via a penalty method.

C. Verification of Adjoint Gradients

The adjoint gradients are verified by comparison to a direct complex variable method. Because both methods use complex variables, their evaluated gradients are expected to agree to several significant figures. The direct complex variable method evaluates the shape sensitivities by sequentially perturbing each design variable in the complex plane, executing the mesh movement routine, and then evaluating the objective function via a converged flow solution. The objective function sensitivity is then given by

$$\frac{\partial J}{\partial \boldsymbol{D}_j} = \frac{\text{Im}[J(\boldsymbol{Q}(\boldsymbol{D}_j + ih), \boldsymbol{X}(\boldsymbol{D}_j + ih))]}{h} \qquad (17)$$

This differs from the adjoint method implemented for this work, in that the adjoint solver uses complex-step differentiation to build the partial derivatives outlined above, and then solves the adjoint system. Further reading on the direct complex variable method can be found in the work by Martins [65]. The chosen geometry and flow conditions are taken from the experimental campaign by Simeonides et al. [66] and are those for the Mach 6, 7.5 deg compression corner. The flow over the model was ideal air. A schematic of the problem is presented in Fig. 9. The wedge surface was parameterized using a 4-point Bézier curve; the first and last points were fixed; the remaining two points, annotated on Fig. 9, were the design variables. The mesh consisted of 50 cells in the x direction and 25 cells in the y direction, with cell stretching in the y direction to capture the boundary layer. Although this mesh is not well resolved for engineering purposes, it serves its purpose to verify the adjoint gradients. The flow solver residuals were converged to machine precision using a constant Courant–Friedrichs–Lewy (CFL) value of 1. Second-order reconstruction was used in conjunction with the limiter freezing method outlined above. The adjoint gradients were evaluated using the frozen limiter values. The direct complex variable approach was initialized with the converged flow state including the frozen limiter values, and the solver was then executed for several thousand more steps until the sensitivity information had converged to machine precision, similar to the approach by Thompson [56]. The blending
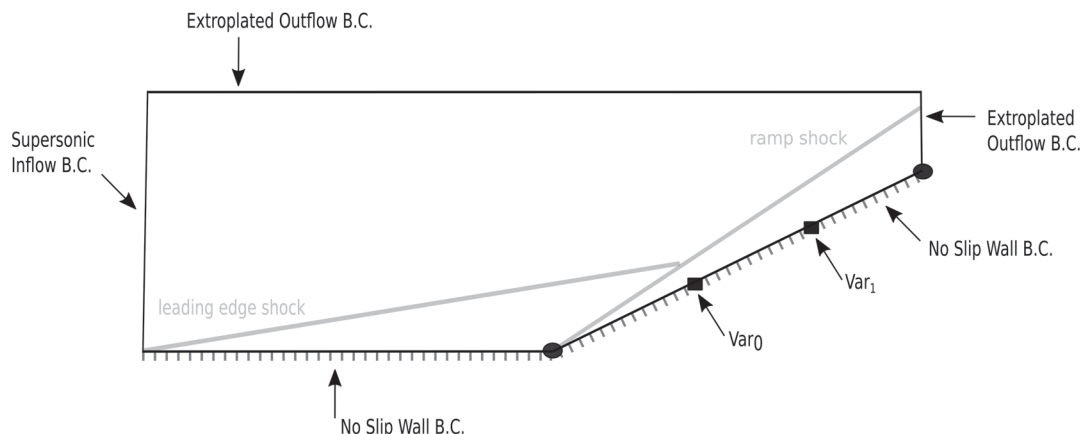

Fig. 9   Schematic of 15 deg flat-plate wedge geometry with Bézier points superimposed on wedge section (∘, fixed-points; ■, design variables) (B.C. = Boundary Condition).

Table 6   Sensitivities of the inviscid drag component acting on the wedge section

Equation	Method	Var_0	Var_1
Euler (SB)	Direct	$-4.594183086029831e+02$	$1.803545660822891e+02$
	Adjoint	$-4.594183086029751e+02$	$1.803545660822925e+02$
Euler (4MB)	Direct	$-4.578044643486712e+02$	$1.795628739115091e+02$
	Adjoint	$-4.578044643486759e+02$	$1.795628739114956e+02$
RANS (SB)	Direct	$-8.683408385995121e+02$	$1.900431473981142e+03$
	Adjoint	$-8.683408385995051e+02$	$1.900431473981131e+03$
RANS (4MB)	Direct	$-8.683156434934184e+02$	$1.900457510584376e+03$
	Adjoint	$-8.683653295253905e+02$	$1.900701298865737e+03$
RANS (8MB)	Direct	$-8.6809937520721110e+02$	$1.9004431301468817e+03$
	Adjoint	$-8.6833107690871600e+02$	$1.9004792612670160e+03$

SB, single block; 4MB, four blocks; 8MB, eight blocks.

parameter (s in Eq. (37) from Wada and Liou [37]) in the AUSMDV flux calculator that blends the AUSMD and AUSMV schemes was set to a fixed value of 0, such that both the AUSMD scheme and AUSMV scheme had equal contributions to the calculated flux. This was to accommodate the direct complex variable solver that was observed to be sensitive to the numerical routine employed in computing this parameter. The adjoint solver was verified for use with the Euler, Navier–Stokes, and RANS equations in `Eilmer`. The sensitivity of the inviscid drag component acting on the wedge section is presented in Table 6. Here we show the results for the Euler and RANS equations. As expected, there is an excellent agreement between the two methods for the Euler and single-block RANS cases. A reduction in accuracy is observed for the multiblock RANS sensitivities, as a result of the simplified boundary implementation outlined in Sec. IV.A. Table 6 shows the effects of the simplification when the domain is decomposed into four and eight blocks. The relative error in Var_0 increased as the number of blocks increased; however, the relative error in Var_1 decreased. The effect of the simplification has been observed to reduce as the number of cells in each block increases because the simplification is applied only at the intersection of a block-to-block boundary condition with a physical boundary condition. Increasing the number of cells in a block effectively decreases the ratio of simplified entries to exact entries in $[\partial \boldsymbol{R} / \partial \boldsymbol{Q}]^T$. To demonstrate that the solver is suitable for a practical decomposition, an additional verification test case was performed using a mesh consisting of 200 cells in the x direction and 100 cells in the y direction decomposed into 32 blocks. The observed relative error for this configuration was of the same order of magnitude as the previous results. It will be demonstrated in Sec. V that this level of accuracy is sufficient for gradient-based optimization.

V.   Design Optimization of the P2 Hypersonic Inlet

The original design objective for the P2 hypersonic inlet was to achieve a compression ratio of 2 across the cowl shock (corresponding to a compression ratio of 6.25 relative to the freestream), while providing a uniform pressure distribution across the throat of the inlet. Our chosen objective function for the redesign of the inlet is presented as Eq. (18).

$$J = \frac{\int_0^H (p(x,y) - p^*)^2 \, dA}{A_{\text{tot}}} \tag{18}$$

Here, $p^* = r_p p_\infty$ is the desired pressure at the throat, and r_p is the desired compression ratio referenced to the freestream pressure. For our design optimization, we set $r_p = 6.25$ and $p_\infty = 701.4$ Pa, to be consistent with the original design objective documented by Gnos et al. [3]. The objective function [Eq. (18)] was evaluated at the baseline inlet throat location, shown in Fig. 10. The design surface was designated as the segment of the body side of the inlet spanning from the end of the fore-body wedge, approximately 1.1 m downstream of the leading edge, to the end of the computational domain. The fore-body wedge and cowl-side geometry act to provide the core-flow compression, and, because the goal is to remove the reflected shock, they remain fixed during the optimization. The design surface segment of inlet was parameterized by an n-order Bézier curve. The initial Bézier control points are fitted to the baseline P2 inlet geometry. To ensure smooth continuity between the fixed inlet surfaces and the design surface, the first, second, and last Bézier control points have fixed y coordinates. The remaining control points have a variable y coordinate. Further details of the parameterization can be found in the Appendix. Figure A1 displays the initial parameterization and the resultant curve for the 11-point Bézier curve and the 20-point Bézier curve. The turbulence properties were chosen to be those of simulation S2, and the optimization was performed on grid level G2. The optimizer was run for a fixed number of design iterations.

Adjoint optimization results for two Bézier curve parameterizations, an 11-point curve and a 20-point curve, are presented here. The Bézier parameters for the baseline and optimized curves can be found in Tables A1 and A2. After 20 objective function evaluations and 4 adjoint solves, the objective function has already been reduced by more than 95% of the original value for both cases. The entire
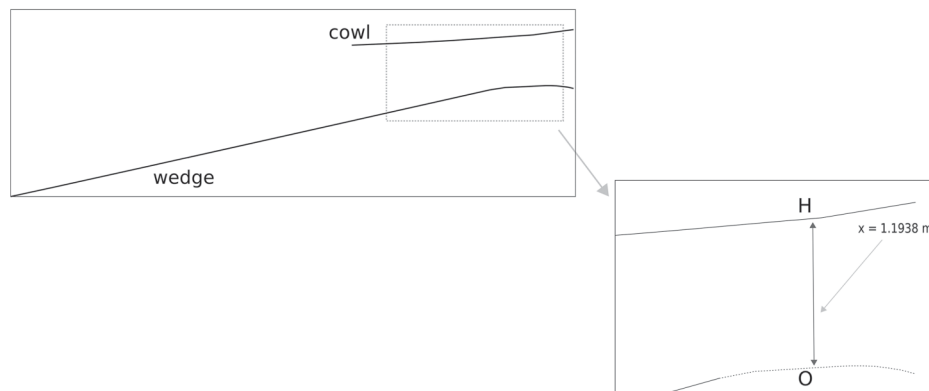

Fig. 10   P2 inlet objective function integral path (design surface shown as dashed line).

optimizer search history is shown in Fig. 11. Also shown in Fig. 11 is the same design problem optimized using standard finite difference gradients with a step size of 1×10^{-3}. Some observations can be made regarding the efficiency of the adjoint approach from the comparison of these results. The number of objective function evaluations required to sufficiently reduce the objective function scales excellently with the number of design variables for the adjoint approach, and little difference is observed in the history of objective function evaluations when comparing 11-point and 20-point adjoint optimizations: on the other hand, the finite difference approach is shown to scale very poorly. Given that, for this particular problem, an adjoint solve costs roughly the same as a flow solve, this demonstrates that the efficiency of the adjoint approach over the finite difference approach is substantial. Furthermore, for the adjoint optimizations, the wall-clock time taken to reach the fixed
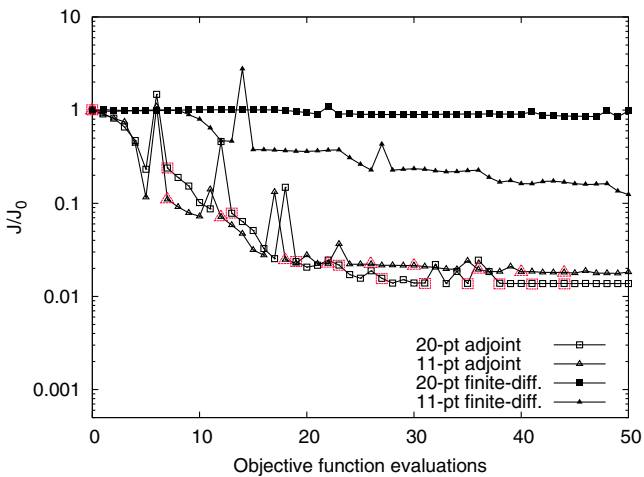
number of design iterations for the two parameterizations was within 2% of each other, where the 11-point optimization (*not* the 20-point optimization) incurred the longer wall-clock time, meaning that the
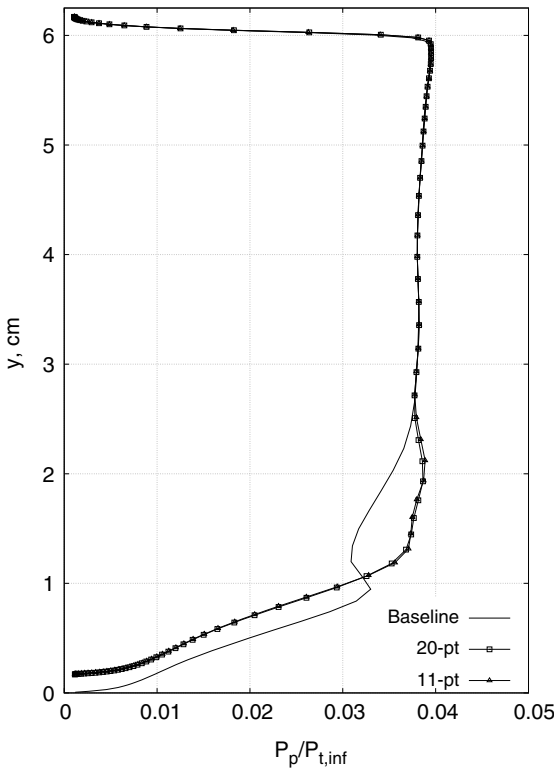

Fig. 11 Objective function history. Symbols with borders denote both an objective function and an adjoint system evaluation.

Fig. 13 Comparison of Pitot pressure P_P at station J, $x = 1.1938$ m, normalized by $P_{t,\infty} = 4.14$ MPa for optimized inlets.
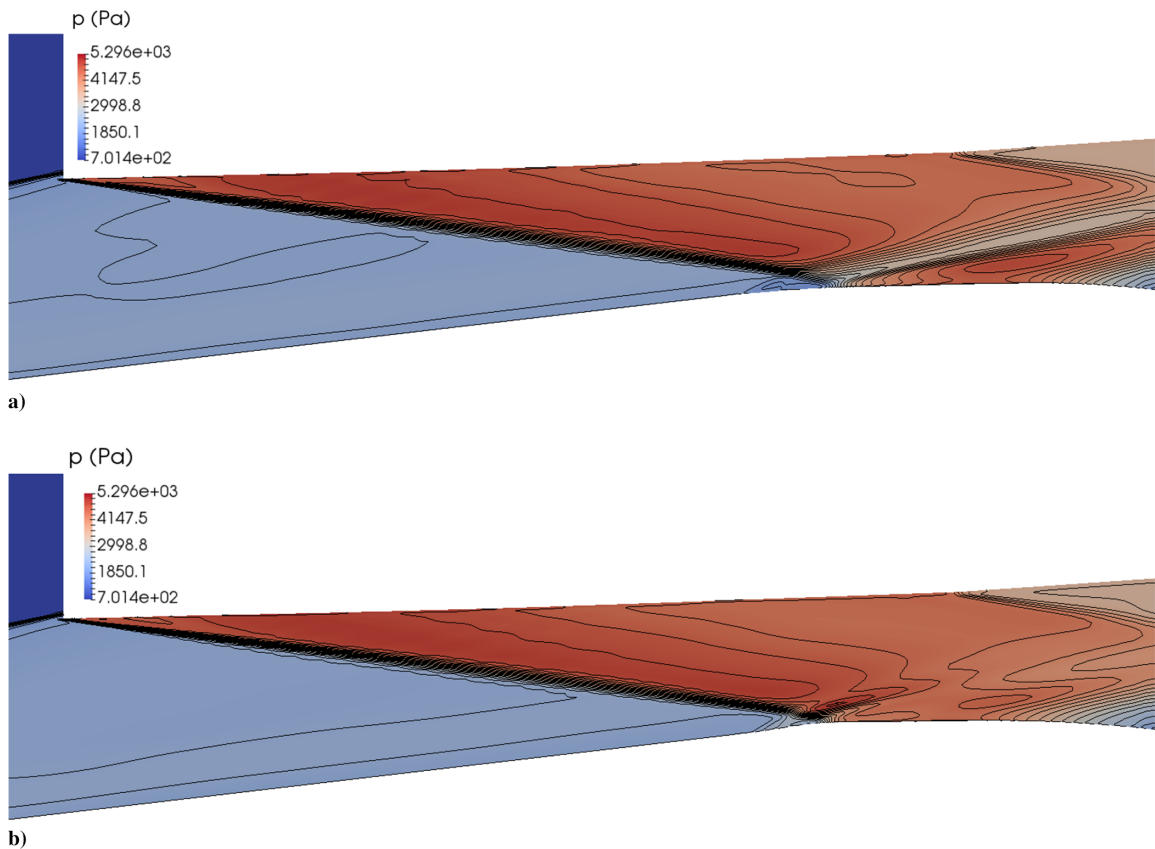

a)

b)

Fig. 12 P2 inlet pressure color map with contour lines overlaid for a) baseline and b) optimized (20-point Bézier curve).
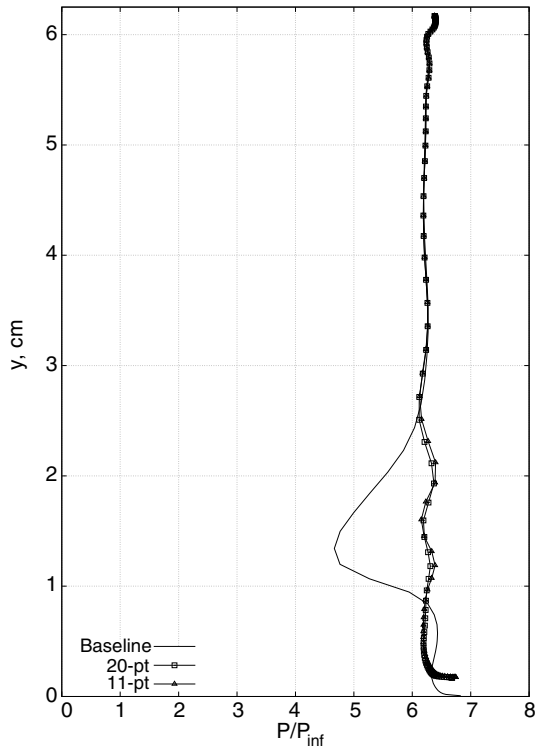
Fig. 14 Comparison of pressure p at station J, $x = 1.1938$ m, normalized by $p_\infty = 701.4$ Pa for optimized inlets.
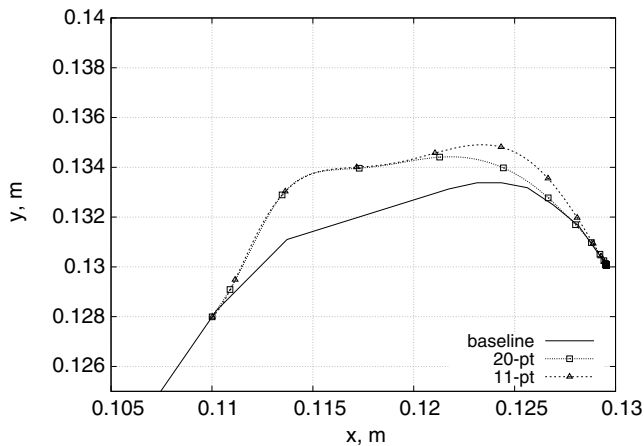

Fig. 15 Comparison of baseline P2 inlet and optimized Bézier curves.

Table 7 Performance metrics at respective throat locations extracted as flux-conserved quantities

Performance metric	Baseline	20-point	11-point
Throat location (x_{throat}, m)	1.1938	1.1447	1.1459
Throat width (Δ_{OH}, mm)	61.18	58.86	58.80
Compression ratio (p/p_∞)	5.987	6.367	6.366
Total pressure recovery ($p_t/p_{t,\infty}$)	0.576	0.584	0.584
Adiabatic kinetic energy efficiency ($\eta_{\text{KE,ad}}$)	0.985	0.985	0.985

difference was not a direct result of the additional design parameters. So, an approximate doubling in the number of design variables has resulted in no additional compute time. This clearly demonstrates the advantage of the adjoint approach over black-box-style gradient-based methods.

Figure 12 presents a pressure color map with contour lines overlaid for the baseline and the 20-point Bézier curve optimized inlet. It is observed that the reflected shock has been virtually removed, without any substantial effects to the upstream flow features of the inlet. Similar pressure fields were obtained for the 11-point Bézier curve optimized inlet, but the plots have been omitted for brevity.

Plots of the Pitot pressure and static pressure normalized by their freestream values at the baseline throat location (J station) are presented in Figs. 13 and 14. It is observed that the characteristic pressure drop, from the shock–boundary-layer interaction, has almost been completely removed for all cases, confirming the removal of the reflected shock. Furthermore, it is evident that similar profiles have been obtained for both the 11-point and 20-point parameterizations. A comparison of the two optimized Bézier curves is presented in Fig. 15. It is observed that both curves share similar profiles up until approximately $x = 1.1938$ m. After this location, the two curves deviate significantly from each other. This result is explainable; because the flow is supersonic in the inlet, perturbations to the geometry downstream of the objective function evaluation location should have negligible effects on the design. This can be confirmed by examining the adjoint variables, which provide the sensitivity to the objective function with respect to conserved residuals in each cell. Figure 16 presents a color map of the adjoint variable related to the conserved mass residual. It is observed that, downstream of the objective function evaluation location, the adjoint variable has a magnitude of zero. This insensitivity to the objective function consequently means that the geometry here may be perturbed without any substantial effect on the objective function, noting that a perturbation in the design variables downstream could potentially result in a nonzero $\partial J/\partial \boldsymbol{D}$ term in Eq. (11).

Table 7 lists a number of performance metrics for the baseline and optimized inlets. The adiabatic energy efficiency is computed from its definition:

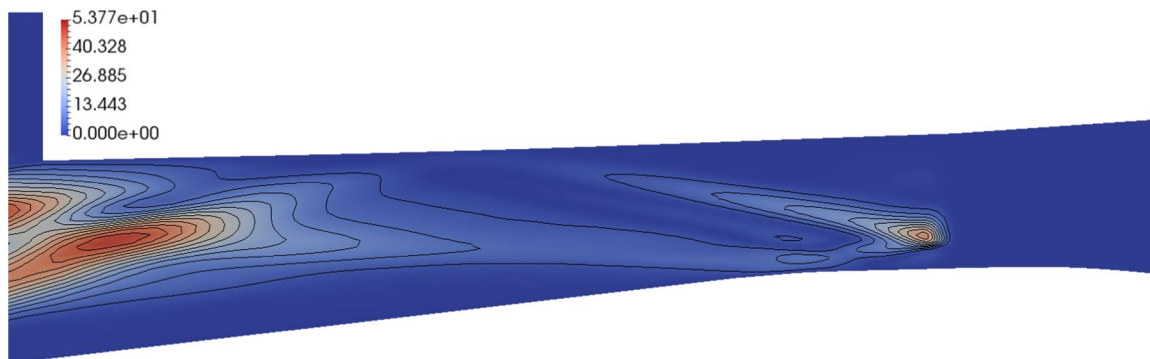$$\eta_{\text{KE,ad}} = \frac{h_{t_0} - h_2'}{h_{t_0} - h_0} \qquad (19)$$

Fig. 16 Color map with contour lines of the absolute value of the adjoint variable related to Eq. (18) and the conserved mass residual for baseline P2 inlet.

where h'_2 is the enthalpy the flow would have if the gas state at the throat were expanded isentropically to the freestream pressure. The throat location has moved upstream by approximately 4% for both designs, and, in addition, the throat width has been reduced by 4%. The total pressure recovery has increased for the optimized inlets, at no cost to the adiabatic kinetic energy efficiency, which has remained constant despite the geometric perturbations, a common trait of $\eta_{KE,ad}$ as discussed in the textbook by Heiser and Pratt ([67] p. 208). Note that the performance metrics in Table 7 were not evaluated at the objective function location, which was set to the baseline throat location. The performance metrics for both redesigns at the baseline throat location were approximately $p/p_\infty = 6.22$, $p_t/p_{t,\infty} = 0.578$, and $\eta_{KE,ad} = 0.985$. Summarizing the results, the new inlets have achieved the desired compression ratio and removed the reflected shock, while retaining or improving the performance metrics.

VI. Conclusions

A complex variable discrete adjoint solver has been implemented into the open-source compressible-flow CFD code `Eilmer`. The adjoint solver has been coupled with a steady-state flow solver, an inverse distance weighting mesh movement algorithm, and an n-order Bézier curve parameterization to form a shape sensitivity analysis package, for design optimization using the DAKOTA optimization software. Results from a verification and validation study of the flow solver have confirmed the accuracy and applicability for applying `Eilmer` in the computation of inlet flows. The adjoint solver was verified by comparison to a direct complex variable method, and excellent agreement in the computed objective function sensitivities was demonstrated. The developed optimization package was applied to the redesign of the P2 hypersonic inlet. The chosen objective function aimed at removing the reflected cowl shock while obtaining the desired compression ratio. P2 inlet redesign results for an 11-point and 20-point Bézier curve parameterization were presented. Both designs remove the reflected shock while achieving the desired compression ratio, at no cost to the inlet performance metrics. The two Bézier curves were found to be similar upstream of the objective function evaluation location, but differed significantly downstream, as a consequence of the supersonic flow. The scalability of the adjoint approach was demonstrated, and results from a finite-difference-based optimization highlighted the efficiency of the adjoint implementation over traditional black-box-styled gradient-based methods. The results from this work show that the adjoint approach applied to the inlet design is promising. Future work should focus on robust methods for achieving acceptable residual convergence of high-order methods on unstructured grids in hypersonic flow.

Appendix: P2 Inlet Design Parameter Details

Table A1 Eleven-point Bézier coordinates for P2 inlet (in meters)

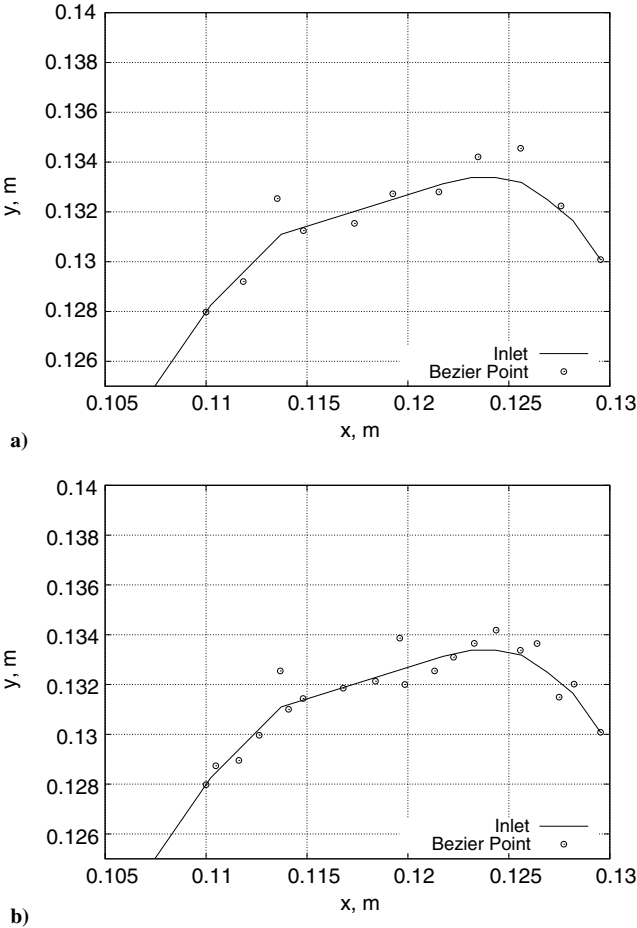| Baseline		Optimized	
x coordinate	y coordinate	x coordinate	y coordinate
1.1000e + 00	1.2798e − 01	1.1000e + 00	1.279e − 01
1.1184e + 00	1.2920e − 01	1.1184e + 00	1.292e − 01
1.1352e + 00	1.3253e − 01	1.1352e + 00	1.3637e − 01
1.1482e + 00	1.3124e − 01	1.1482e + 00	1.3543e − 01
1.1734e + 00	1.3153e − 01	1.1734e + 00	1.3240e − 01
1.1925e + 00	1.3272e − 01	1.1925e + 00	1.3307e − 01
1.2153e + 00	1.3280e − 01	1.2153e + 00	1.3485e − 01
1.2347e + 00	1.3420e − 01	1.2347e + 00	1.3665e − 01
1.2558e + 00	1.3455e − 01	1.2558e + 00	1.3589e − 01
1.2758e + 00	1.3223e − 01	1.2758e + 00	1.3261e − 01
1.2954e + 00	1.3008e − 01	1.2954e + 00	1.3008e − 01

Fig. A1 P2 inlet Bézier parameterization: a) 11-point curve and b) 20-point curve.

Table A2 Twenty-point Bézier coordinates for P2 inlet (in meters)

Baseline		Optimized	
x coordinate	y coordinate	x coordinate	y coordinate
1.1000e + 00	1.2798e − 01	1.1000e + 00	1.2798e − 01
1.1048e + 00	1.2873e − 01	1.1048e + 00	1.2873e − 01
1.1162e + 00	1.2895e − 01	1.1162e + 00	1.2919e − 01
1.1263e + 00	1.2996e − 01	1.1263e + 00	1.3171e − 01
1.1367e + 00	1.3254e − 01	1.1367e + 00	1.3560e − 01
1.1480e + 00	1.3143e − 01	1.1480e + 00	1.3484e − 01
1.1408e + 00	1.3100e − 01	1.1408e + 00	1.3373e − 01
1.1679e + 00	1.3180e − 01	1.1679e + 00	1.3357e − 01
1.1839e + 00	1.3213e − 01	1.1839e + 00	1.3334e − 01
1.1984e + 00	1.3200e − 01	1.1984e + 00	1.3339e − 01
1.1959e + 00	1.3386e − 01	1.1959e + 00	1.3565e − 01
1.2132e + 00	1.3254e − 01	1.2132e + 00	1.3442e − 01
1.2225e + 00	1.3309e − 01	1.2225e + 00	1.3459e − 01
1.2328e + 00	1.3365e − 01	1.2328e + 00	1.3456e − 01
1.2436e + 00	1.3418e − 01	1.2436e + 00	1.3461e − 01
1.2556e + 00	1.3337e − 01	1.2556e + 00	1.3352e − 01
1.2639e + 00	1.3364e − 01	1.2639e + 00	1.3368e − 01
1.2748e + 00	1.3149e − 01	1.2748e + 00	1.3149e − 01
1.2822e + 00	1.3201e − 01	1.2822e + 00	1.3201e − 01
1.2954e + 00	1.3008e − 01	1.2954e + 00	1.3008e − 01

References

[1] Smart, M. K., and Tetlow, M. R., "Orbital Delivery of Small Payloads Using Hypersonic Airbreathing Propulsion," *Journal of Spacecraft and Rockets*, Vol. 46, No. 1, 2009, pp. 117–125.
https://doi.org/10.2514/1.38784

[2] Landsberg, W. O., Wheatley, V., and Veeraragavan, A., "Characteristics of Cascaded Fuel Injectors Within an Accelerating Scramjet Combustor," *AIAA Journal*, Vol. 54, No. 12, 2016, pp. 3692–3700.
https://doi.org/10.2514/1.J054815

[3] Gnos, A. V., Watson, E. C., Seebaugh, W. R., Sanator, R. J., and DeCarlo, J. P., "Investigation of Flow Fields Within Large Scale Hypersonic Inlet Models," NASA TN D-7150, 1973.

[4] Smart, M., "Design of Three-Dimensional Hypersonic Inlets with Rectangular-to-Elliptical Shape Transition," *Journal of Propulsion and Power*, Vol. 15, No. 3, 1999, pp. 408–416.
https://doi.org/10.2514/2.5459

[5] Gollan, R., Gollan, R., Ferlemann, P., and Ferlemann, P., "Investigation of REST-Class Hypersonic Inlet Designs," *17th AIAA International Space Planes and Hypersonic Systems and Technologies Conference*, AIAA Paper 2011-2254, 2011.
https://doi.org/10.2514/6.2011-2254

[6] Gelsey, A., Knight, D., Gao, S., and Schwabacher, M., "NPARC Simulation and Redesign of the NASA P2 Hypersonic Inlet," *31st Joint Propulsion Conference and Exhibit*, AIAA Paper 1995-2760, 1995.
https://doi.org/10.2514/6.1995-2760

[7] Shukla, V., Gelsey, A., Schwabacher, M., Smith, D., and Knight, D., "Automated Redesign of the NASA P8 Hypersonic Inlet Using Numerical Optimization," *32nd Joint Propulsion Conference and Exhibit*, AIAA Paper 1996-2549, 1996.
https://doi.org/10.2514/6.1996-2549

[8] Shukla, V., Gelsey, A., Schwabacher, M., Smith, D., and Knight, D. D., "Automated Design Optimization for the P2 and P8 Hypersonic inlets," *Journal of Aircraft*, Vol. 34, No. 2, 1997, pp. 228–235.
https://doi.org/10.2514/2.2161

[9] Hasegawa, S., and Knight, D., "Numerical Analysis and Optimization of Two-Dimensional Hypersonic Inlets," *42nd AIAA Aerospace Sciences Meeting and Exhibit*, AIAA Paper 2004-856, 2004.
https://doi.org/10.2514/6.2004-856

[10] Hasegawa, S., and Knight, D., "Application of Optimization Algorithms to Scramjet Inlet Design," *AIAA/CIRA 13th International Space Planes and Hypersonics Systems and Technologies Conference*, AIAA Paper 2005-3207, 2005.
https://doi.org/10.2514/6.2005-3207

[11] Drayna, T. W., "Design and Optimization of Hypersonic Inward-Turning Inlets," Ph.D. Thesis, Univ. of Minnesota, Minneapolis, MN, 2011.

[12] Ferlemann, P. G., and Gollan, R. J., "Parametric Geometry, Structured Grid Generation, and Initial Design Study for REST-Class Hypersonic Inlets," *JANNAF 43rd Combustion & 31st Airbreathing Joint Meeting*, Joint Army Navy NASA Air Force (JANNAF), La Jolla, CA, 2010.

[13] Pironneau, O., "On Optimum Design in Fluid Mechanics," *Journal of Fluid Mechanics*, Vol. 64, No. 1, 1974, pp. 97–110.
https://doi.org/10.1017/S0022112074002023

[14] Thévenin, D., and Janiga, G., *Optimization and Computational Fluid Dynamics*, Springer Science & Business Media, New York, 2008, pp. 80–83, Chap. 4.

[15] Lee, B. J., and Kim, C., "Aerodynamic Redesign Using Discrete Adjoint Approach on Overset Mesh System," *Journal of Aircraft*, Vol. 45, No. 5, 2008, pp. 1643–1653.
https://doi.org/10.2514/1.34112

[16] Kline, H. L., Palacios, F., and Alonso, J. J., "Sensitivity of the Performance of a 3-Dimensional Hypersonic Inlet to Shape Deformations," *19th AIAA International Space Planes and Hypersonic Systems and Technologies Conference*, AIAA Paper 2014-3228, 2014.
https://doi.org/10.2514/6.2014-3228

[17] Kline, H. L., Palacios, F., Economon, T. D., and Alonso, J. J., "Adjoint-Based Optimization of a Hypersonic Inlet," *22nd AIAA Computational Fluid Dynamics Conference*, AIAA Paper 2015-3060, 2015.
https://doi.org/10.2514/6.2015-3060

[18] Kline, H. L., Economon, T. D., and Alonso, J. J., "Mulit-Objective Optimization of a Hypersonic Inlet Using Generalized Outflow Boundary Conditions in the Continuous Adjoint Method," *54th AIAA Aerospace Sciences Meeting*, AIAA Paper 2016-0912, 2016.
https://doi.org/10.2514/6.2016-0912

[19] Kline, H. L., "The Continuous Adjoint Method for Multi-Fidelity Hypersonic Inlet Design," Ph.D. Thesis, Stanford Univ., Stanford, CA, 2017.

[20] Kline, H., and Alonso, J., "Adjoint of Generalized Outflow-Based Functionals Applied to Hypersonic Inlet Design," *AIAA Journal*, Vol. 55, No. 11, 2017, pp. 3903–3915.
https://doi.org/10.2514/1.J055863

[21] Anderson, W. K., and Venkatakrishnan, V., "Aerodynamic Design Optimization on Unstructured Grids with a Continuous Adjoint Formulation," *Computers & Fluids*, Vol. 28, Nos. 4–5, 1999, pp. 443–480.
https://doi.org/10.1016/S0045-7930(98)00041-3

[22] Reuther, J., Jameson, A., Farmer, J., Martinelli, L., and Saunders, D., "Aerodynamic Shape Optimization of Complex Aircraft Configurations via an Adjoint Formulation," *34th Aerospace Sciences Meeting and Exhibit*, AIAA Paper 1996-94, 1996.
https://doi.org/10.2514/6.1996-94

[23] Nadarajah, S., and Jameson, A., "A Comparison of the Continuous and Discrete Adjoint Approach to Automatic Aerodynamic Optimization," *38th Aerospace Sciences Meeting and Exhibit*, AIAA Paper 2000-667, 2000.
https://doi.org/10.2514/6.2000-667

[24] Nielsen, E. J., and Kleb, W. L., "Efficient Construction of Discrete Adjoint Operators on Unstructured Grids Using Complex Variables," *AIAA Journal*, Vol. 44, No. 4, 2006, pp. 827–836.
https://doi.org/10.2514/1.15830

[25] Anderson, W. K., Newman, J. C., Whitfield, D. L., and Nielsen, E. J., "Sensitivity Analysis for Navier-Stokes Equations on Unstructured Meshes Using Complex Variables," *AIAA Journal*, Vol. 39, No. 1, 2001, pp. 56–63.
https://doi.org/10.2514/2.1270.

[26] Burdyshaw, C. E., and Anderson, W. K., "A General and Extensible Unstructured Mesh Adjoint Method," *Journal of Aerospace Computing, Information, and Communication*, Vol. 2, No. 10, 2005, pp. 401–413.
https://doi.org/10.2514/1.15932

[27] Burdyshaw, C. E., "Achieving Automatic Concurrency Between Computational Field Solvers and Adjoint Sensitivity Codes," Ph.D. Thesis, Computational Engineering, Univ. of Tennessee, Chattanooga, TN, 2006.

[28] Martins, J. R. R. A., Sturdza, P., and Alonso, J., "The Connection Between the Complex-Step Derivative Approximation and Algorithmic Differentiation," *39th Aerospace Sciences Meeting and Exhibit*, AIAA Paper 2001-921, 2001.
https://doi.org/10.2514/6.2001-921

[29] Martins, J. R., Sturdza, P., and Alonso, J. J., "The Complex-Step Derivative Approximation," *ACM Transactions on Mathematical Software (TOMS)*, Vol. 29, No. 3, 2003, pp. 245–262.
https://doi.org/10.1145/838250.838251

[30] Gauger, N. R., Walther, A., Moldenhauer, C., and Widhalm, M., "Automatic Differentiation of an Entire Design Chain for Aerodynamic Shape Optimization," edited by C. Tropea, S. Jakirlic, H. J. Heinemann, R. Henke, and H. Hönlinger, *New Results in Numerical and Experimental Fluid Mechanics VI*, Notes on Numerical Fluid Mechanics and Multidisciplinary Design (NNFM), Vol. 96, Springer, Berlin, 2007, pp. 454–461.
https://doi.org/10.1007/978-3-540-74460-3_56

[31] Giles, M., Ghate, D., and Duta, M. C., "Using Automatic Differentiation for Adjoint CFD Code Development," Oxford Univ. Research Archive Rept. 05/25, Oxford, 2005.

[32] Martins, J., Kroo, I., and Alonso, J., "An Automated Method for Sensitivity Analysis Using Complex Variables," *38th Aerospace Sciences Meeting and Exhibit*, AIAA Paper 2000-689, 2000.
https://doi.org/10.2514/6.2000-689

[33] Mader, C. A., Martins, J. R. A., Alonso, J. J., and Der Weide, E. V., "ADjoint: An Approach for the Rapid Development of Discrete Adjoint Solvers," *AIAA Journal*, Vol. 46, No. 4, 2008, pp. 863–873.
https://doi.org/10.2514/1.29123

[34] Albring, T. A., Sagebaum, M., and Gauger, N. R., "Development of a Consistent Discrete Adjoint Solver in an Evolving Aerodynamic Design Framework," *16th AIAA/ISSMO Multidisciplinary Analysis and Optimization Conference*, AIAA Paper 2015-3240, 2015.
https://doi.org/10.2514/6.2015-3240

[35] Jacobs, P., and Gollan, R., "Implementation of a Compressible-Flow Simulation Code in the D Programming Language," *Applied Mechanics*

and Materials, Vol. 846, 2016, pp. 54–60.
https://doi.org/10.4028/www.scientific.net/AMM.846.54

[36] Bright, W., "The D Programming Language," 2018, http://dlang.org.

[37] Wada, Y., and Liou, M.-S., "A Flux Splitting Scheme with High-Resolution and Robustness for Discontinuities," *32nd Aerospace Sciences Meeting and Exhibit*, AIAA Paper 1994-83, 1994.
https://doi.org/10.2514/6.1994-83

[38] Damm, K., Gollan, R., and Jacobs, P., "Verification of the Least-Squares Procedure within an Unstructured-Grid Flow Solver," *20th Australasian Fluid Mechanics Conference*, Univ. of Western Australia, Perth, WA, 2016, Paper 703.

[39] Venkatakrishnan, V., "On the Accuracy of Limiters and Convergence to Steady State Solutions," *31st Aerospace Sciences Meeting*, AIAA Paper 1993-880, 1993.
https://doi.org/10.2514/6.1993-880

[40] Haselbacher, A., and Blazek, J., "On the Accurate and Efficient Discretisation of the Navier-Stokes Equations on Mixed Grids," *14th Computational Fluid Dynamics Conference*, AIAA Paper 1999-3363, 1999.
https://doi.org/10.2514/6.1999-3363

[41] Wilcox, D. C., *Turbulence Modeling for CFD*, Vol. 3, DCW Industries, La Canada, CA, 2006, pp. 84–87, Chap. 4.

[42] Chan, W., Jacobs, P., and Mee, D., "Suitability of the $k - \omega$ Turbulence Model for Scramjet Flowfield Simulations," *International Journal for Numerical Methods in Fluids*, Vol. 70, No. 4, 2012, pp. 493–514.
https://doi.org/10.1002/fld.v70.4

[43] Coratekin, T., Keuk, J. V., and Ballman, J., "Performance of Upwind Schemes and Turbulence Models in Hypersonic Flows," *AIAA Journal*, Vol. 42, No. 5, 2004, pp. 945–957.
https://doi.org/10.2514/1.9588

[44] Knoll, D. A., and Keyes, D. E., "Jacobian-Free Newton–Krylov Methods: A Survey of Approaches and Applications," *Journal of Computational Physics*, Vol. 193, No. 2, 2004, pp. 357–397.
https://doi.org/10.1016/j.jcp.2003.08.010

[45] Saad, Y., *Iterative Methods for Sparse Linear Systems*, Vol. 82, SIAM, Philadelphia, Pennsylvania, 2003, pp. 92–95, 301–311, Chap. 3, 10.

[46] Roache, P. J., and Steinberg, S., "Symbolic Manipulation and Computational Fluid Dynamics," *AIAA Journal*, Vol. 22, No. 10, 1984, pp. 1390–1394.
https://doi.org/10.2514/3.8794

[47] Oberkampf, W. L., and Roy, C. J., *Verification and Validation in Scientific Computing*, Cambridge Univ. Press, New York, 2010, pp. 210–234, Chap. 6.

[48] Roy, C., Tendean, E., Veluri, S., Rifki, R., Luke, E., and Hebert, S., "Verification of RANS Turbulence Models in Loci-CHEM Using the Method of Manufactured Solutions," *18th AIAA Computational Fluid Dynamics Conference*, AIAA Paper 2007-4203, 2007.
https://doi.org/10.2514/6.2007-4203

[49] Ghia, U., Bayyuk, S., Habchi, S., Roy, C., Shih, T., Conlisk, T., Hirsch, C., and Powers, J. M., "The AIAA Code Verification Project-Test Cases for CFD Code Verification," *48th AIAA Aerospace Sciences Meeting Including the New Horizons Forum and Aerospace Exposition*, AIAA Paper 2010-125, 2010.
https://doi.org/10.2514/6.2010-125

[50] Knight, D. D., "Numerical Simulation of Realistic High-Speed Inlets Using the Navier-Stokes Equations," *AIAA Journal*, Vol. 15, No. 11, 1977, pp. 1583–1589.
https://doi.org/10.2514/3.60825

[51] Various, "Air Intakes for High Speeds Vehicles," Advisory Group for Aerospace Research and Development Rept. AGARD-AG-270, NATO, Nice, France, 1991.

[52] Squire, W., and Trapp, G., "Using Complex Variables to Estimate Derivatives of Real Functions," *SIAM Review*, Vol. 40, No. 1, 1998, pp. 110–112.
https://doi.org/10.1137/S003614459631241X

[53] Vanden, K. J., and Orkwis, P. D., "Comparison of Numerical and Analytical Jacobians," *AIAA Journal*, Vol. 34, No. 6, 1996, pp. 1125–1129.
https://doi.org/10.2514/3.13202

[54] Saad, Y., "Krylov Subspace Methods in Distributed Computing Environments," Army High Performance Computing Center Tech. Rept. TR-92-126, Stanford, CA, 1992.

[55] Rizk, M., "The Use of Finite-Differenced Jacobians for Solving the Euler Equations and for Evaluating Sensitivity Derivatives," *Fluid Dynamics Conference*, AIAA Paper 1994-2213, 1994.
https://doi.org/10.2514/6.1994-2213

[56] Thompson, K. B., "Aerothermodynamic Design Sensitivities for a Reacting Gas Flow Solver on an Unstructured Mesh Using a Discrete Adjoint Formulation," Ph.D. Thesis, North Carolina State Univ., Raleigh, NC, 2017.

[57] White, J. A., Baurle, R. A., Passe, B. J., Spiegel, S. C., and Nishikawa, H., "Geometrically Flexible and Efficient Flow Analysis of High Speed Vehicles via Domain Decomposition, Part 1: Unstructured-Grid Solver for High Speed Flows," *2017 JANNAF—Interagency Propulsion Committee Meeting*, Joint Army Navy NASA Air Force (JANNAF), Newport News, VA, 2017.

[58] Venkatakrishnan, V., "Convergence to Steady State Solutions of the Euler Equations on Unstructured Grids with Limiters," *Journal of Computational Physics*, Vol. 118, No. 1, 1995, pp. 120–130.
https://doi.org/10.1006/jcph.1995.1084

[59] Van Albada, G., Van Leer, B., and Roberts, W., "A Comparative Study of Computational Methods in Cosmic Gas Dynamics," *Upwind and High-Resolution Schemes*, Springer, Berlin, 1997, pp. 95–103.
https://doi.org/10.1007/978-3-642-60543-7_6

[60] Van Leer, B., "Towards the Ultimate Conservative Difference Scheme. V. A Second-Order Sequel to Godunov's Method," *Journal of Computational Physics*, Vol. 32, No. 1, 1979, pp. 101–136.
https://doi.org/10.1016/0021-9991(79)90145-1

[61] Witteveen, J., "Explicit and Robust Inverse Distance Weighting Mesh Deformation for CFD," *48th AIAA Aerospace Sciences Meeting Including the New Horizons Forum and Aerospace Exposition*, AIAA Paper 2010-165, 2010.
https://doi.org/10.2514/6.2010-165

[62] Karypis, G., and Kumar, V., "MeTis: Unstructured Graph Partitioning and Sparse Matrix Ordering System, Version 4.0," 2009, http://www.cs.umn.edu/metis.

[63] Adams, B., Bauman, L., Bohnhoff, W., Dalbey, K., Ebeida, M., Eddy, J., Eldred, M., Hough, P., Hu, K., and Jakeman, J., "Dakota: A Multilevel Parallel Object-Oriented Framework for Design Optimization, Parameter Estimation, Etc: Version 6 User's Manual," Sandia National Lab. Tech. Rept. SAND2014-4633, Albuquerque, New Mexico, 2015.

[64] Fletcher, R., and Reeves, C. M., "Function Minimization by Conjugate Gradients," *Computer Journal*, Vol. 7, No. 2, 1964, pp. 149–154.
https://doi.org/10.1093/comjnl/7.2.149

[65] Martins, J. R., "A Coupled-Adjoint Method for High-Fidelity Aero-Structural Optimization," Ph.D. Thesis, Stanford Univ., Stanford, CA, 2002.

[66] Simeonides, G., Haase, W., and Manna, M., "Experimental, Analytical, and Computational Methods Applied to Hypersonic Compression Ramp Flows," *AIAA Journal*, Vol. 32, No. 2, 1994, pp. 301–310.
https://doi.org/10.2514/3.11985

[67] Heiser, W. H., and Pratt, D. T., *Hypersonic Airbreathing Propulsion*, AIAA, Reston, VA, 1994, pp. 207–208, Chap. 5.

P. J. Drummond
Associate Editor